Electronic Supplementary Material (ESI) for Dalton Transactions.

"Cadmium and manganese hypophosphite perovskites templated by formamidinium cations: dielectric, optical and magnetic properties"

by Mirosław Mączka, Dagmara Stefańska, Maciej Ptak, Anna Gągor, Adam Pikul and Adam Sieradzki

Table S1. Experimental details

For all structures: $CH_{11}CdN_2O_6P_3$, M_r = 352.43, Z = 4. Experiments were carried out with Mo $K\alpha$ radiation using a Xcalibur, Atlas. Absorption was corrected for by multi-scan methods, *CrysAlis PRO* 1.171.38.41 (Rigaku Oxford Diffraction, 2015). Empirical absorption correction using spherical harmonics, implemented in SCALE3 ABSPACK scaling algorithm.

	PhaseI	PhaseII
Crystal data		
Crystal system, space group	Monoclinic, *C*2/*c*	Monoclinic, $P2_1/n$
Temperature (K)	295	100
a, *b*, *c* (Å)	13.6653 (4), 10.3708 (3), 7.5573 (3)	13.7142 (2), 10.3493 (3), 7.4175 (5)
β (°)	103.058 (3)	103.390 (4)
V (Å^3)	1043.33 (6)	1024.16 (8)
μ (mm^{-1})	2.55	2.60
Crystal size (mm)	0.18 × 0.13 × 0.08	0.18 × 0.13 × 0.08
Data collection		
T_{min}, T_{max}	0.853, 1.000	0.780, 1.000
No. of measured, independent and observed [$I > 2\sigma(I)$] reflections	13593, 1384, 1225	24109, 2090, 1646
R_{int}	0.030	0.044
$(\sin\theta/\lambda)_{max}$ (Å^{-1})	0.692	0.625
Refinement		
$R[F^2 > 2\sigma(F^2)]$, $wR(F^2)$, S	0.018, 0.046, 1.07	0.028, 0.058, 1.08
No. of reflections	1384	2090
No. of parameters	81	155
$\Delta\rangle_{max}$, $\Delta\rangle_{min}$ (e Å^{-3})	0.41, -0.35	0.75, -0.63

Computer programs: *CrysAlis PRO* 1.171.38.41 (Rigaku OD, 2015), *SHELXT* 2014/5 (Sheldrick, 2014), *SHELXL2018*/3 (Sheldrick, 2018).

Table S2. Selected geometric parameters (Å, º)

Phase I, 295 K		*Phase II, 100 K*	
Cd1—O1	2.2756 (18)	Cd1—O1	2.274 (3)
Cd1—O1^{i}	2.2757 (18)	Cd1—O3	2.274 (2)
Cd1—O2	2.2820 (13)	Cd1—O5	2.276 (2)
Cd1—O2^{i}	2.2820 (13)	Cd1—O2^{vi}	2.280 (3)
Cd1—O3^{ii}	2.2867 (14)	Cd1—O4^{iii}	2.290 (2)
Cd1—O3^{iii}	2.2867 (14)	Cd1—O6^{vii}	2.297 (2)
P2—O3	1.4893 (15)	P1—O1	1.486 (3)
P2—O2	1.5020 (15)	P1—O2	1.493 (3)
P1—O1^{iv}	1.4794 (18)	P2—O4	1.500 (2)
P1—O1	1.4794 (18)	P2—O3	1.515 (2)
N1—C1	1.307 (5)	P3—O6	1.500 (2)
N2—C1	1.279 (6)	P3—O5	1.514 (2)
		N1A—C1A	1.319 (10)
		N2A—C1A	1.290 (13)
		N2B—C1B	1.285 (18)
O1—Cd1—O1^{i}	180.00 (9)	O1—Cd1—O3	88.56 (9)
O1—Cd1—O2	87.51 (7)	O1—Cd1—O5	90.98 (9)
O1^{i}—Cd1—O2	92.49 (7)	O3—Cd1—O5	178.96 (8)
O1—Cd1—O2^{i}	92.49 (7)	O1—Cd1—O2^{vi}	178.57 (11)
O1^{i}—Cd1—O2^{i}	87.51 (7)	O3—Cd1—O2^{vi}	92.24 (9)
O2—Cd1—O2^{i}	180.0	O5—Cd1—O2^{vi}	88.24 (9)
O1—Cd1—O3^{ii}	91.40 (7)	O1—Cd1—O4^{iii}	90.82 (10)
O1^{i}—Cd1—O3^{ii}	88.60 (7)	O3—Cd1—O4^{iii}	89.27 (8)
O2—Cd1—O3^{ii}	90.61 (5)	O5—Cd1—O4^{iii}	89.80 (8)
O2^{i}—Cd1—O3^{ii}	89.39 (5)	O2^{vi}—Cd1—O4^{iii}	90.38 (10)
O1—Cd1—O3^{iii}	88.60 (7)	O1—Cd1—O6^{vii}	89.95 (10)
O1^{i}—Cd1—O3^{iii}	91.40 (7)	O3—Cd1—O6^{vii}	90.70 (8)
O2—Cd1—O3^{iii}	89.39 (5)	O5—Cd1—O6^{vii}	90.23 (8)
O2^{i}—Cd1—O3^{iii}	90.61 (5)	O2^{vi}—Cd1—O6^{vii}	88.85 (10)
O3^{ii}—Cd1—O3^{iii}	180.00 (9)	O4^{iii}—Cd1—O6^{vii}	179.23 (10)
O3—P2—O2	118.25 (9)	O1—P1—O2	115.19 (15)
O1^{iv}—P1—O1	114.66 (15)	O4—P2—O3	117.39 (14)
P2—O2—Cd1	131.89 (9)	O6—P3—O5	117.79 (14)
P2—O3—Cd1^{v}	132.80 (9)	P1—O1—Cd1	143.09 (16)
P1—O1—Cd1	142.49 (11)	P1—O2—Cd1^{viii}	139.36 (16)

N2—C1—N1	121.6 (4)	P2—O3—Cd1	129.55 (13)
		P2—O4—Cd1^{v}	132.69 (13)
		P3—O5—Cd1	129.47 (13)
		P3—O6—Cd1^{ix}	130.65 (13)
		N2A—C1A—N1A	122.9 (8)

Symmetry code(s): (i) -*x*+3/2, -*y*+3/2, -*z*+1; (ii) *x*, -*y*+1, *z*-1/2; (iii) -*x*+3/2, *y*+1/2, -*z*+3/2; (iv) -*x*+1, *y*, -*z*+1/2; (v) -*x*+3/2, *y*-1/2, -*z*+3/2; (vi) *x*+1/2, -*y*+3/2, *z*+1/2; (vii) -*x*+3/2, *y*-1/2, -*z*+1/2; (viii) *x*-1/2, -*y*+3/2, *z*-1/2; (ix) -*x*+3/2, *y*+1/2, -*z*+1/2.

Table S3. Distortion Parameters in selected hypophosphites, Δd - bond length distortion; σ^2 octahedral angle variance [1].

Compound	T (K)	Space group	Independent Mn Centres	σ^2 (°)	$\Delta d \cdot 10^{-5}$
$[MHy]Mn(H_2POO)_3$	295	*Pnma*	1	8.7	3.0
$[MHy]Mn(H_2POO)_3$	100	*Pnma*	1	8.4	3.5
$[DMA]Mn(H_2POO)_3$	298	$P2_1/c$	1	4.1	3.3
			2	9.0	7.8
			3	9.1	2.6
$[FA]Mn(H_2POO)_3$	295	*C*2/*c*	1	3.3	0.09
$[FA]Mn(H_2POO)_3$	115	$P2_1/n$	1	4.5	7.7
$[GUA]Mn(H_2POO)_3$	298	*I*2/*m*	1	2.3	32.0
$[GUA]Mn(H_2POO)_3$	302	*P*-1	1	13.5	8.7
			2	4.7	7.1
$[FA]Cd(H_2POO)_3$	295	*C*2/*c*	1	3.1	0.4
$[FA]Cd(H_2POO)_3$	100	$P2_1/n$	1	1.4	1.5

Table S4. Selected hydrogen-bond parameters

D*—H···*A	***D*—H (Å)**	**H···*A* (Å)**	***D*···*A* (Å)**	***D*—H···*A* (°)**
PhaseI				
N1—H1A···O2	0.86	2.01	2.843 (2)	162.1
N1—H1B···O2^{i}	0.86	2.07	2.843 (2)	148.9
N2—H2A···O3^{ii}	0.86	1.99	2.831 (5)	164.4
N2—H2B···O1^{iii}	0.86	2.45	3.247 (5)	154.6
N2—H2B···O1^{iv}	0.86	2.22	2.936 (5)	141.1
C1—H1C···O3^{v}	0.93	2.26	3.185 (4)	173.5
PhaseII				
N1A—H1A1···O5^{vi}	0.86	1.99	2.820 (3)	163.2
N2A—H2A1···O6^{viii}	0.86	2.01	2.852 (7)	167.5
N2A—H2A2···O1^{viii}	0.86	2.30	2.968 (7)	135.0
N2A—H2A2···O2^{viii}	0.86	2.34	3.154 (7)	159.1
C1A—H1A···O4	0.93	2.22	3.152 (10)	175.4
N1B—H1B1···O3^{vii}	0.86	1.99	2.824 (3)	163.1
N2B—H2B1···O4	0.86	2.00	2.847 (9)	167.9
N2B—H2B2···O1^{viii}	0.86	2.53	3.335 (9)	156.2
N2B—H2B2···O2^{viii}	0.86	2.15	2.859 (10)	139.3
C1B—H1B···O6^{viii}	0.93	2.23	3.158 (13)	176.0

Symmetry code(s): (i) -*x*+1, *y*, -*z*+3/2; (ii) -*x*+3/2, *y*+1/2, -*z*+3/2; (iii) -*x*+1, -*y*+2, -*z*+1; (iv) *x*, -*y*+2, *z*+1/2; (v) *x*-1/2, *y*+1/2, *z*; (vi) -*x*+2, -*y*+1, -*z*+1; (vii) -*x*+3/2, *y*-1/2, -*z*+3/2; (viii) *x*+1/2, -*y*+3/2, *z*+1/2.

Table S5. Raman wavenumbers (cm^{-1}) of the $[FA]Cd(H_2POO)_3$ perovskite together with proposed assignment of observed bands.

300 K	80 K	Assignment
3310w	3318w	$\nu(NH_2)$
3211w	3220w	$\nu(NH_2)$
3095w	3088w	$\nu(NH_2)$
3007w	2999w	$\nu(CH)$
	2402w	$\nu_s(PH_2)$
2377 vs	2394vs+2382vs	$\nu_s(PH_2)$
	2366w	$\nu_s(PH_2)$
2341m	2343m	$\nu_{as}(PH_2)$
2316m	2320m	$\nu_{as}(PH_2)$
2306m	2310m	$\nu_{as}(PH_2)$
2273w	2271w	$\nu_{as}(PH_2)$
1406m	1401m	$\delta(CH)$
1368vw	1384w	$\rho(NH_2)$
1164s	1175m+1167s	$\nu_{as}(PO_2)+\delta(PH_2)$
1143s	1148w+1140s	$\nu_{as}(PO_2)+\nu_s(CN)$
1132sh	1133sh+1128sh	$\nu_{as}(PO_2)$
1093w	1102w+1086w	$\nu_s(PO_2)+\omega(PH_2)$
1069s	1069s+1065sh	$\nu_s(PO_2)$
1039s	1044s+1033s	$\nu_s(PO_2)$
942m	956m+939m	$\tau(PH_2)$
895w	892w	$\tau(PH_2)$
816m	823m	$\rho(PH_2)$
807w	808m+802m	$\rho(PH_2)$
689vw,vb	729 m	$\omega(NH_2)$
566w	561w	$\delta(NCN)$
500m	499m	$\delta(PO_2)$
471w	472m	$\delta(PO_2)$

456m	453m	$\delta(PO_2)$
290m	310m	$T'(Cd^{2+})$
	289w	$T'(Cd^{2+})$
240w	261w	$T'(Cd^{2+})+T'(H_2POO^-)$
	234w+221w	$T'(Cd^{2+})+T'(H_2POO^-)$
	180w	$T(H_2POO^-)$
150m	164vw+154m+136m	$T'(FA^+)+L(H_2POO^-)$
105m	111m+103sh+95w	$L(FA^+)+L(H_2POO^-)$
60w	85w+76w+65w	$L(H_2POO^-)$

[a]Key: vs, very strong; s, strong; m, medium; w, weak; vw, very weak; vb, very broad; ν_s, symmetric stretching; ν_{as}, antisymmetric stretching; δ, bending (scissoring) or in-plane bending; ρ, rocking; ω, wagging; τ, twisting; T', translation; L, libration.

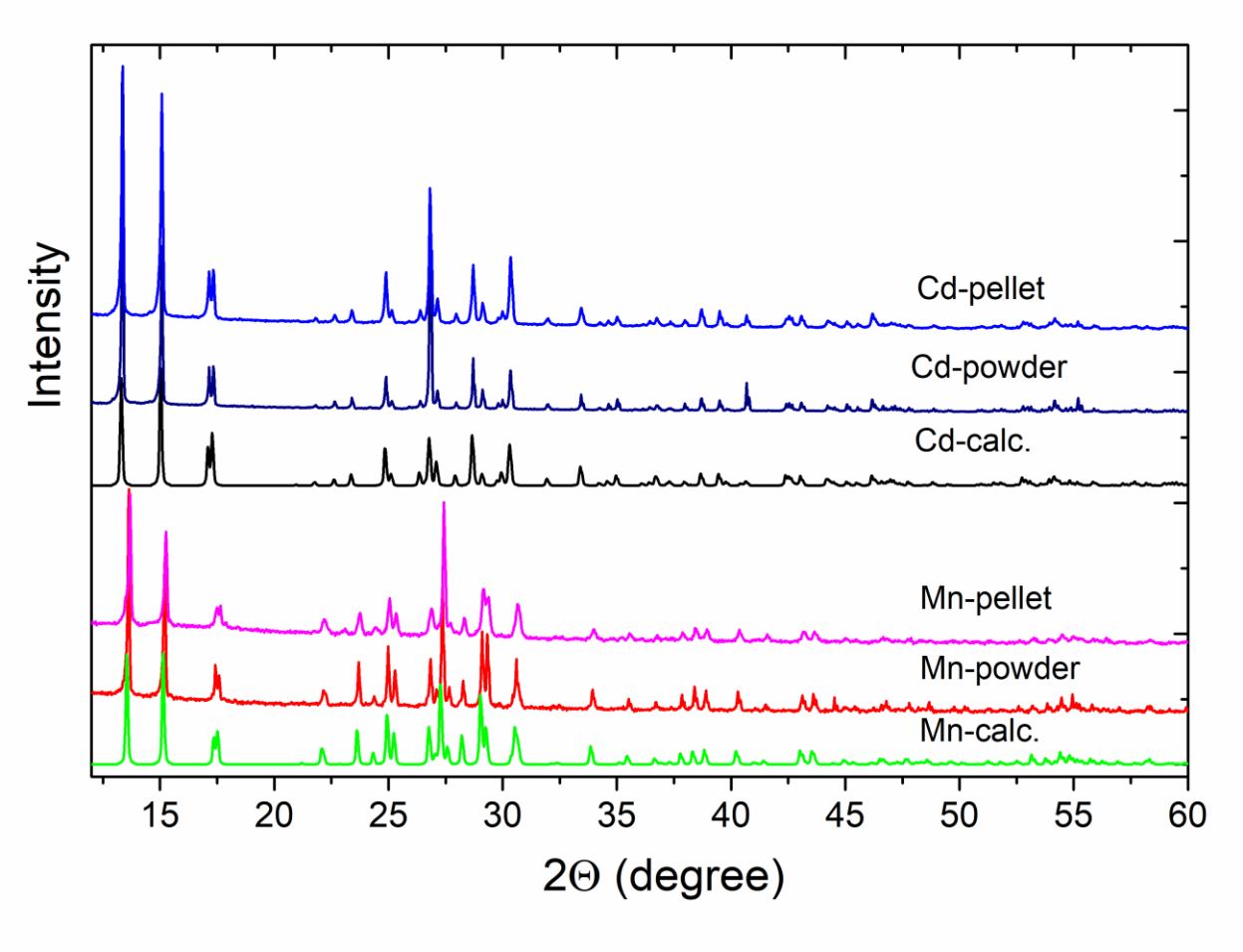

Figure S1. Experimental XRD patterns of powdered [FA]M($H_2POO)_3$ (M=Mn, Cd) and pressed samples (pellets) together with the calculated ones based on the RT crystal structures.

(a) Phase I, C2/c 295K; only h+k=2n peaks are present

(b) Phase II, $P2_1/n$, 100 K; diffraction peaks breaking the reflection conditions for C-centered lattice, h+k=2n+1

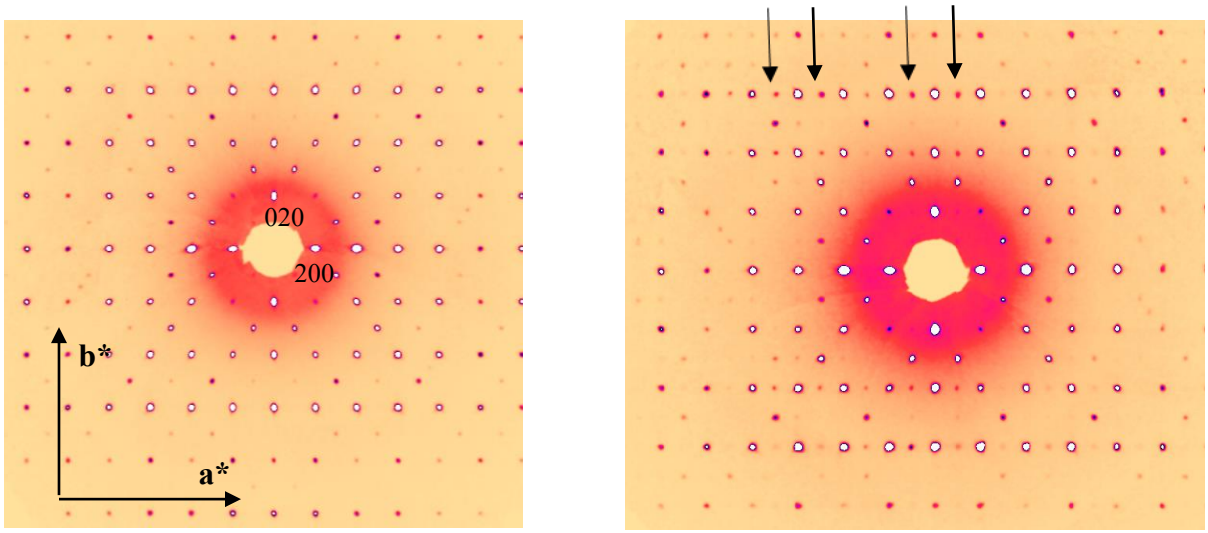

(c) diffraction pictures taken below and abowe the phase transition temperature confirm symmetry changes

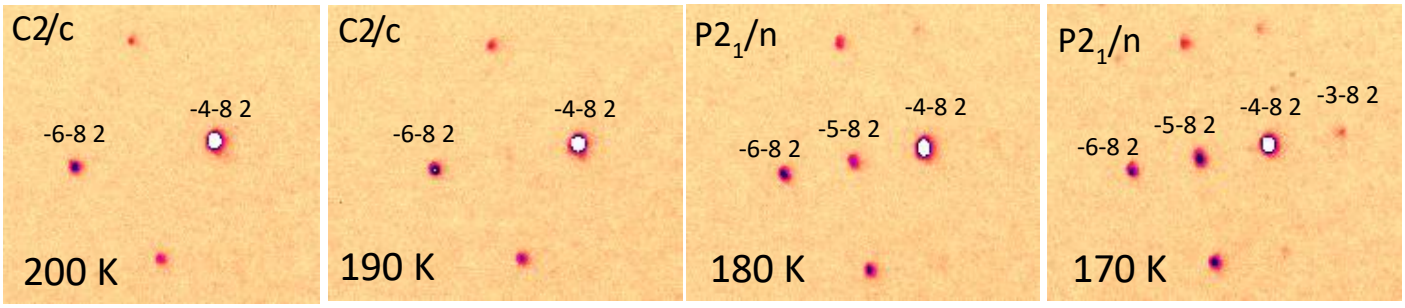

(d)

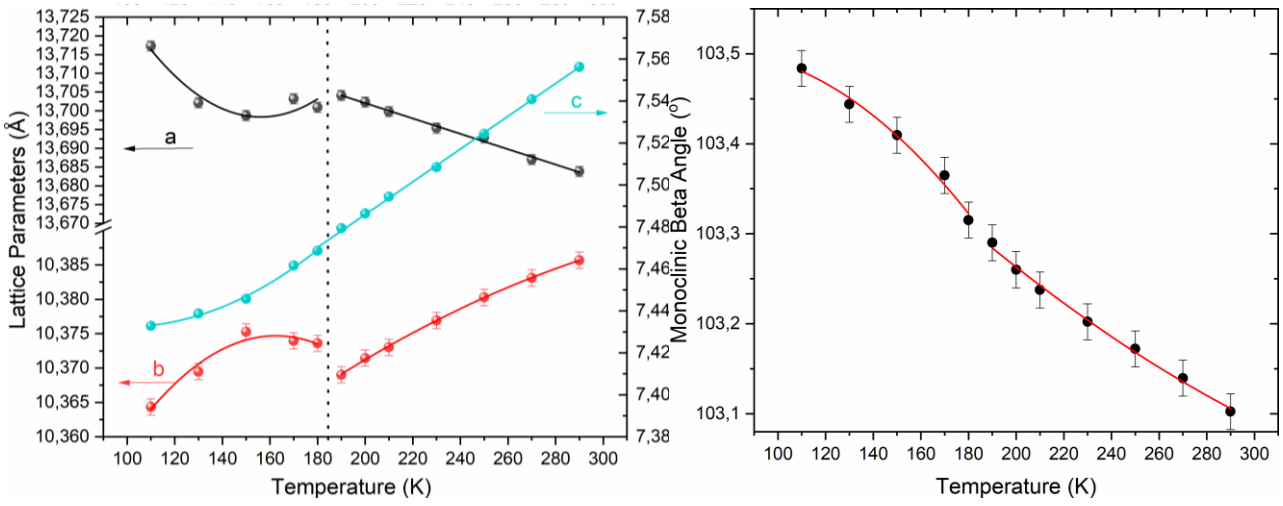

Figure S2. (a)-(b) hk0 reciprocal planes in both phases of $[FA]Cd(H_2POO)_3$; (c) diffraction images near the phase transition temperature; (d) temperature evolution of lattice parameters.

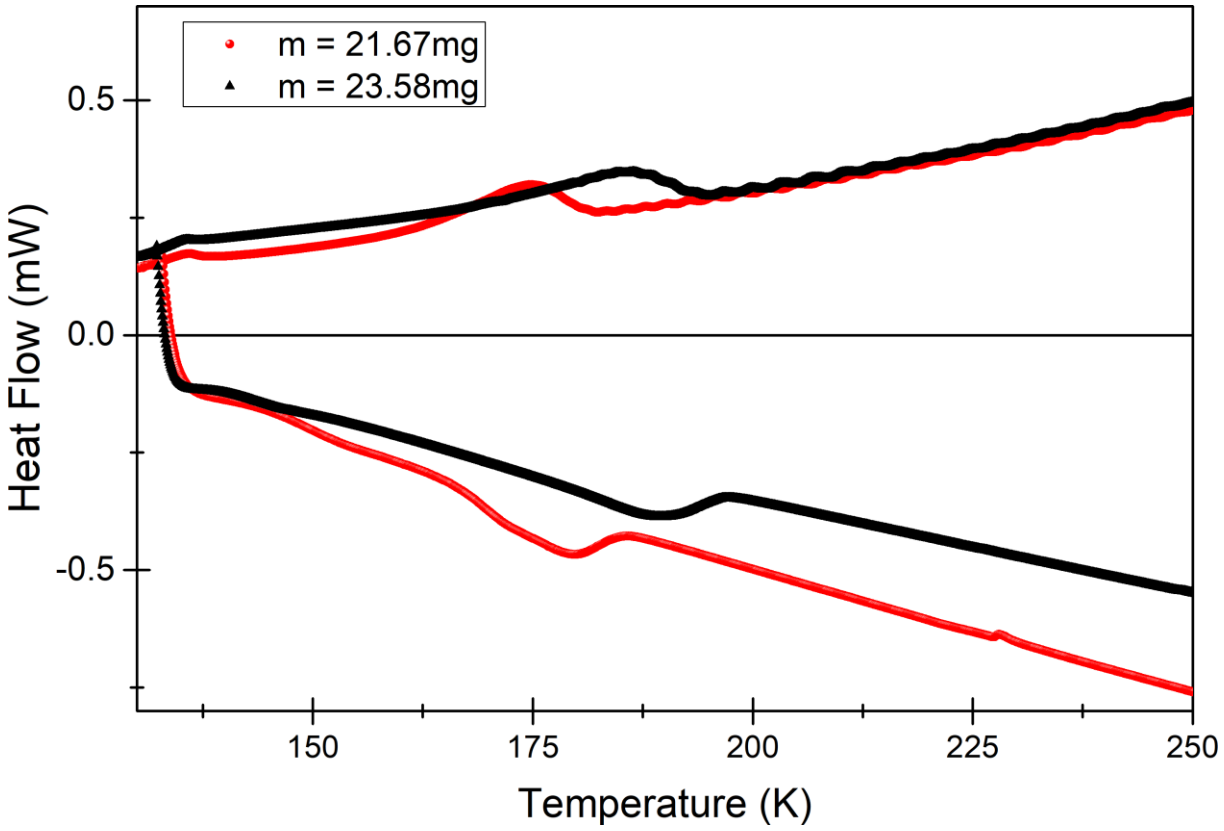

Figure S3. DSC traces of [FA]Cd(H_2POO)$_3$ (black) and [FA]Mn(H_2POO)$_3$ (red).

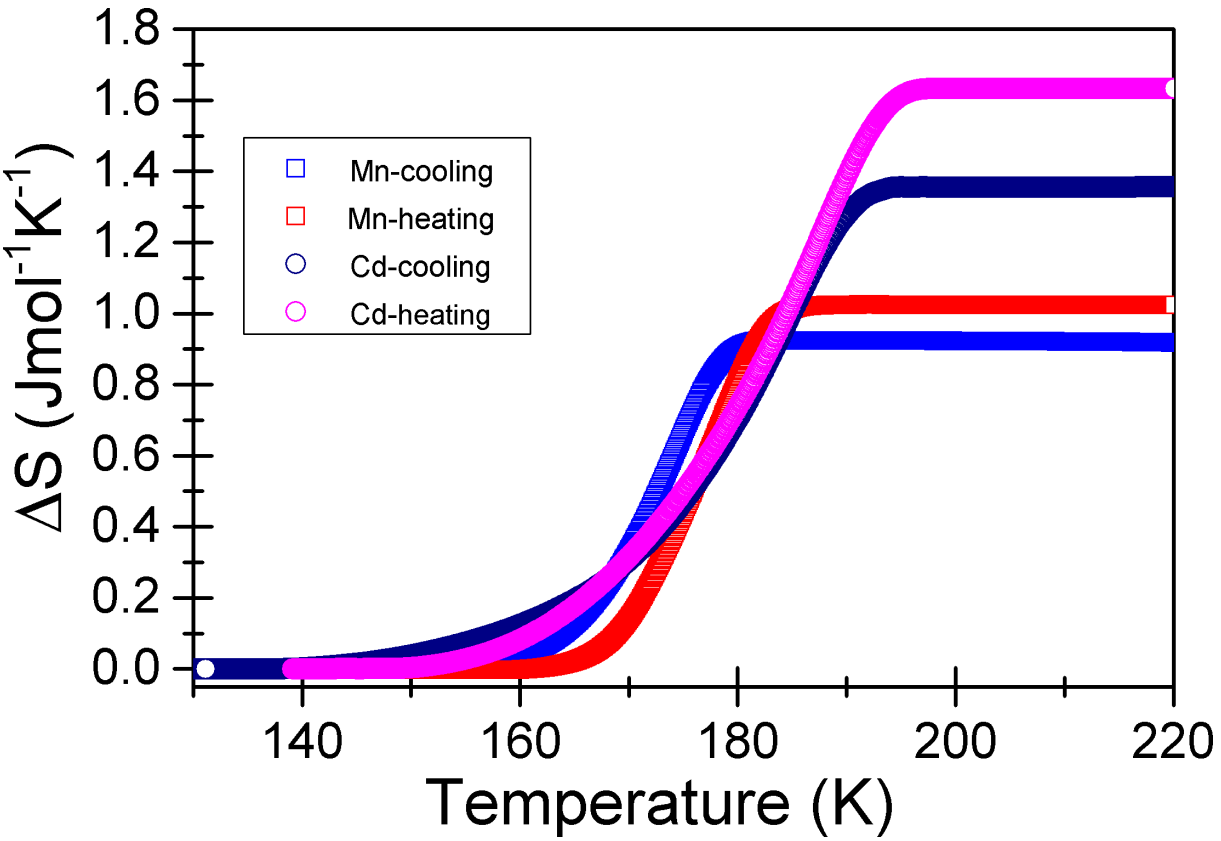

Figure S4. Temperature dependence of ΔS related to the phase transitions in the Mn (squares) and Cd (circles) analogue in heating (red and magenta) and cooling (blue and navy) runs.

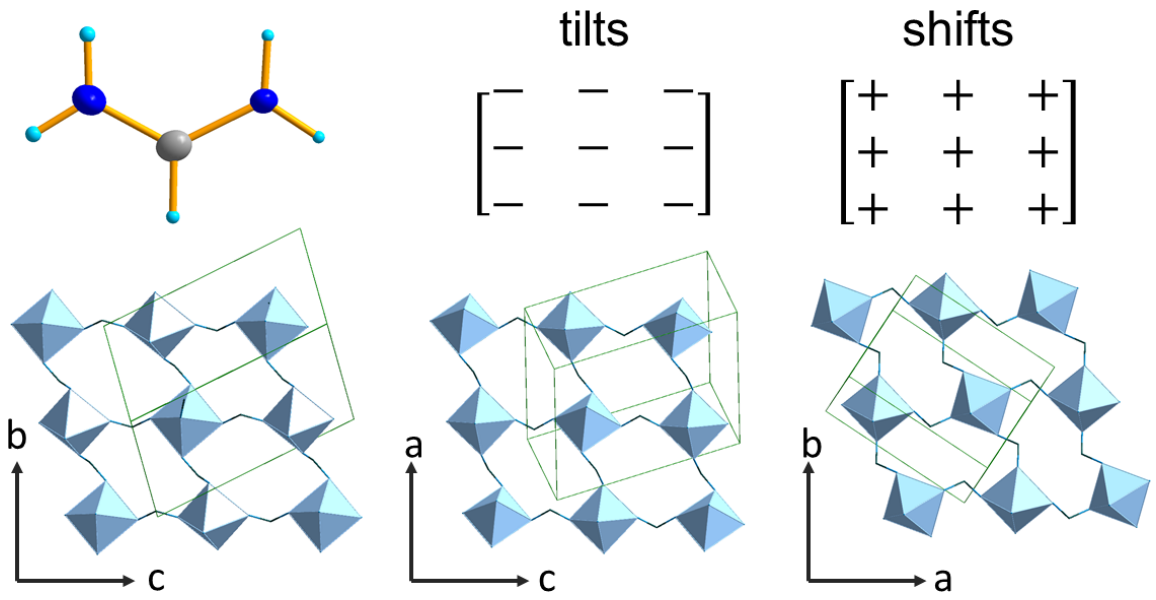

Figure S5. Tilts and shifts [2,3] in monoclinic [FA]Cd($H_2POO)_3$ polymorph. Axes demonstrate pseudo-cubic directions; (above) FA^+ with tilt and shift matrixes; (below) single 3 x 3 layers. The green cell refers to the monoclinic unit cell.

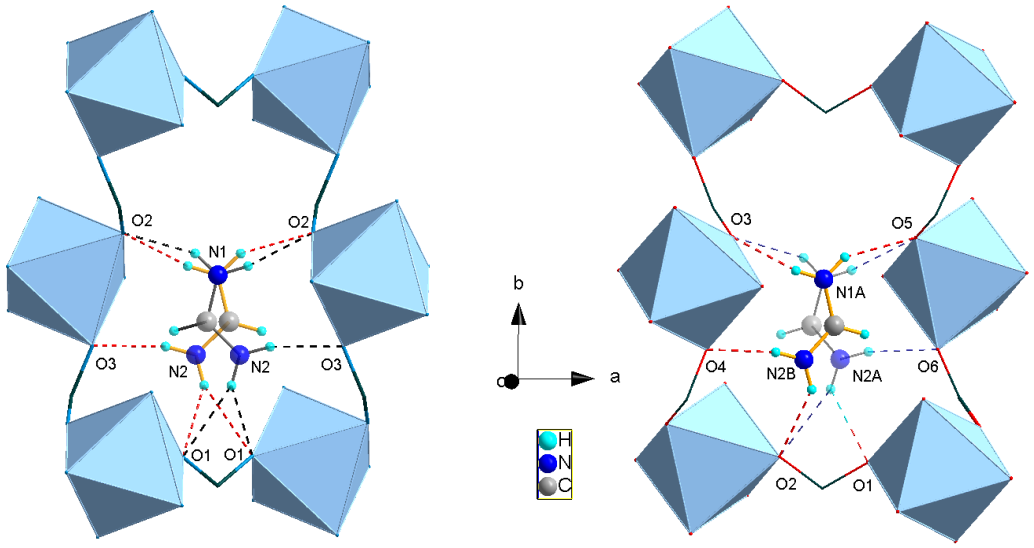

Figure S6. N-H···O HBs in the high (on the left) and low (on the right) temperature polymorphs with atom numbering scheme. The site occupation factors in phase I are equal to 0.5 for both placements in II it is equal to 0.4 and 0.6 for A and B amines, respectively.

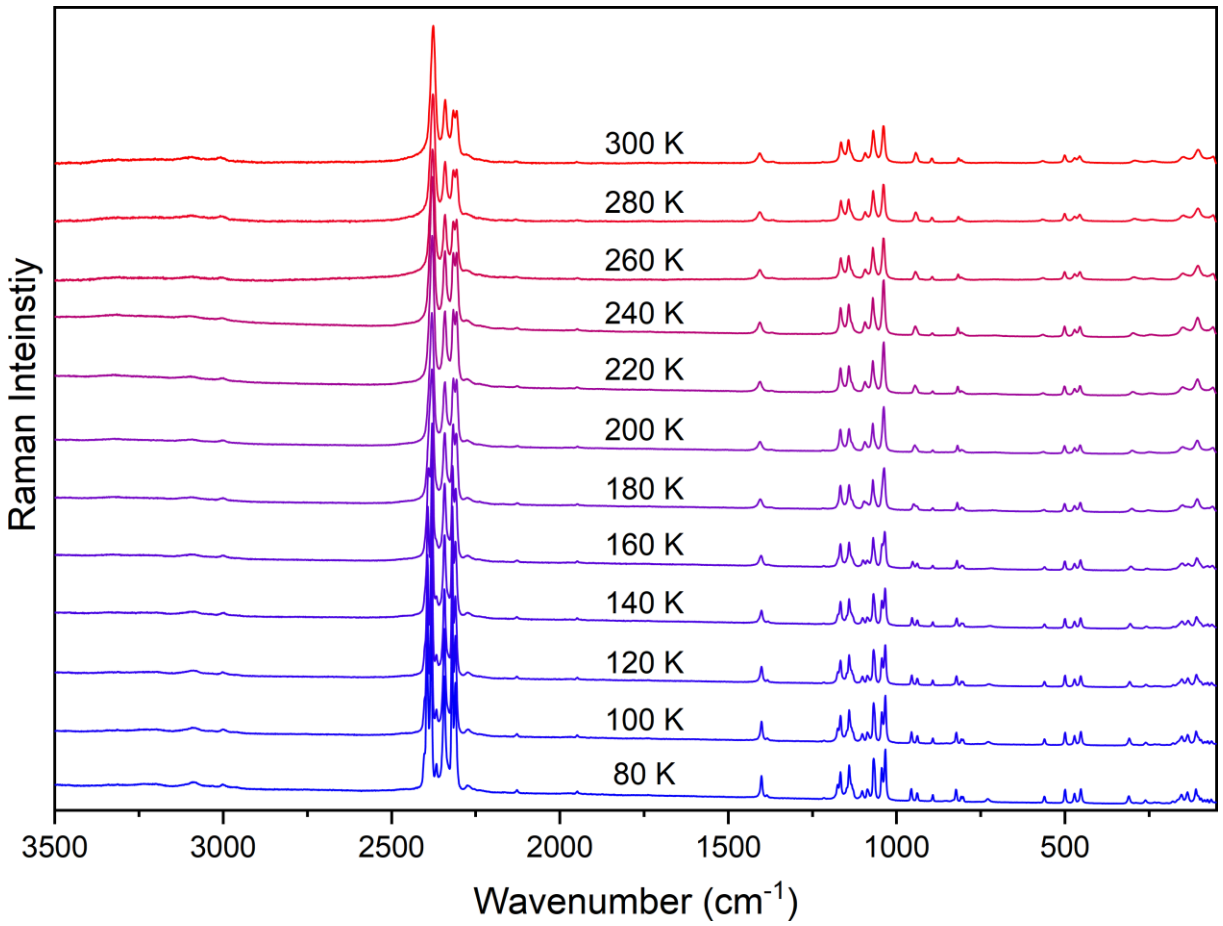

Figure S7. Temperature-dependent Raman spectra of [FA]Cd($H_2POO)_3$ in the whole wavenumber range.

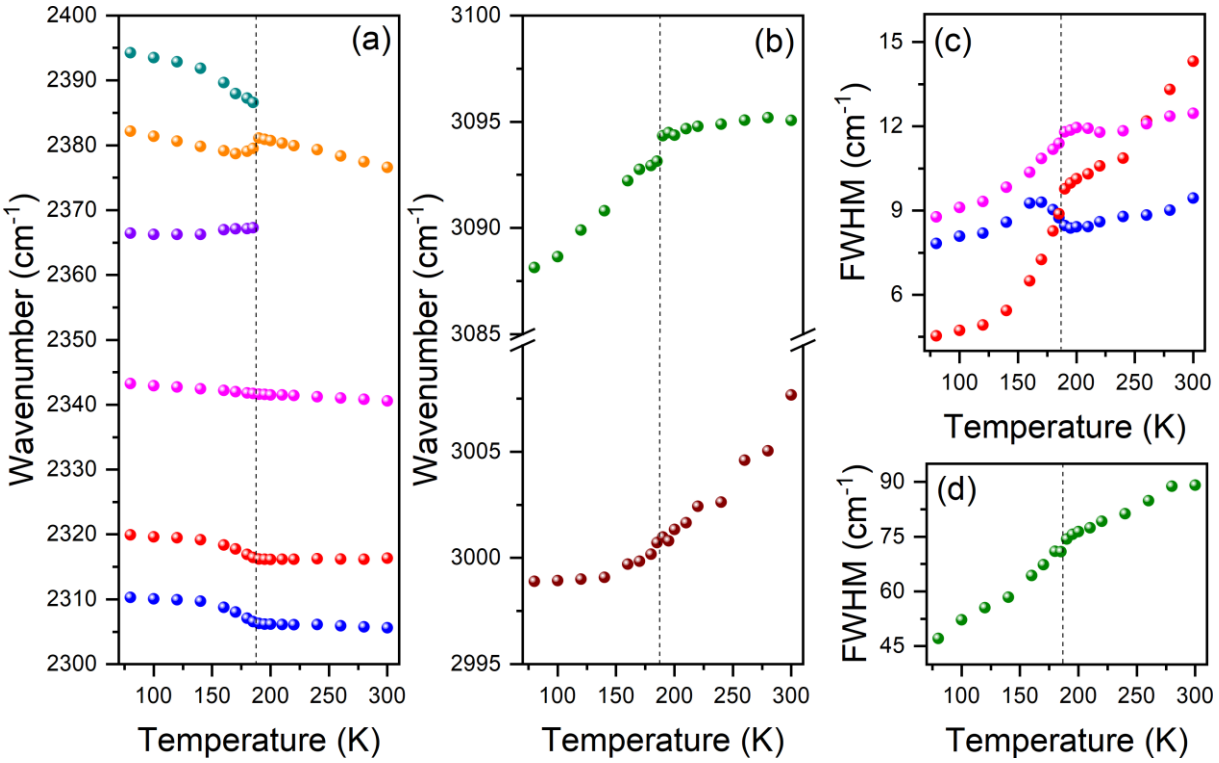

Figure S8. Temperature dependence of wavenumbers (a and b) and FWHM (c and d) for selected PH_2, NH_2 and CH stretching modes.

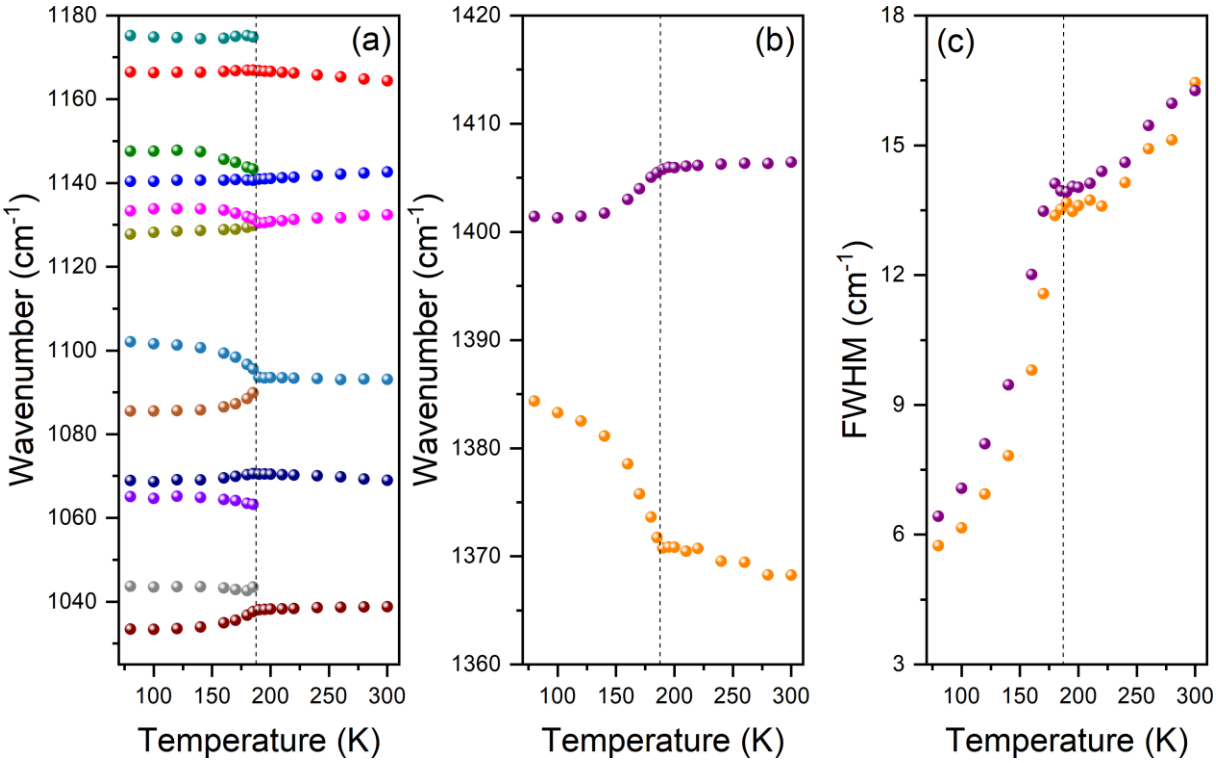

Figure S9. Temperature dependence of wavenumbers for PO_2 stretching modes (a). Panels (b) and (c) show temperature dependence of wavenumbers and FWHM, respectively, for $\rho(NH_2)$ and δ(CH) modes.

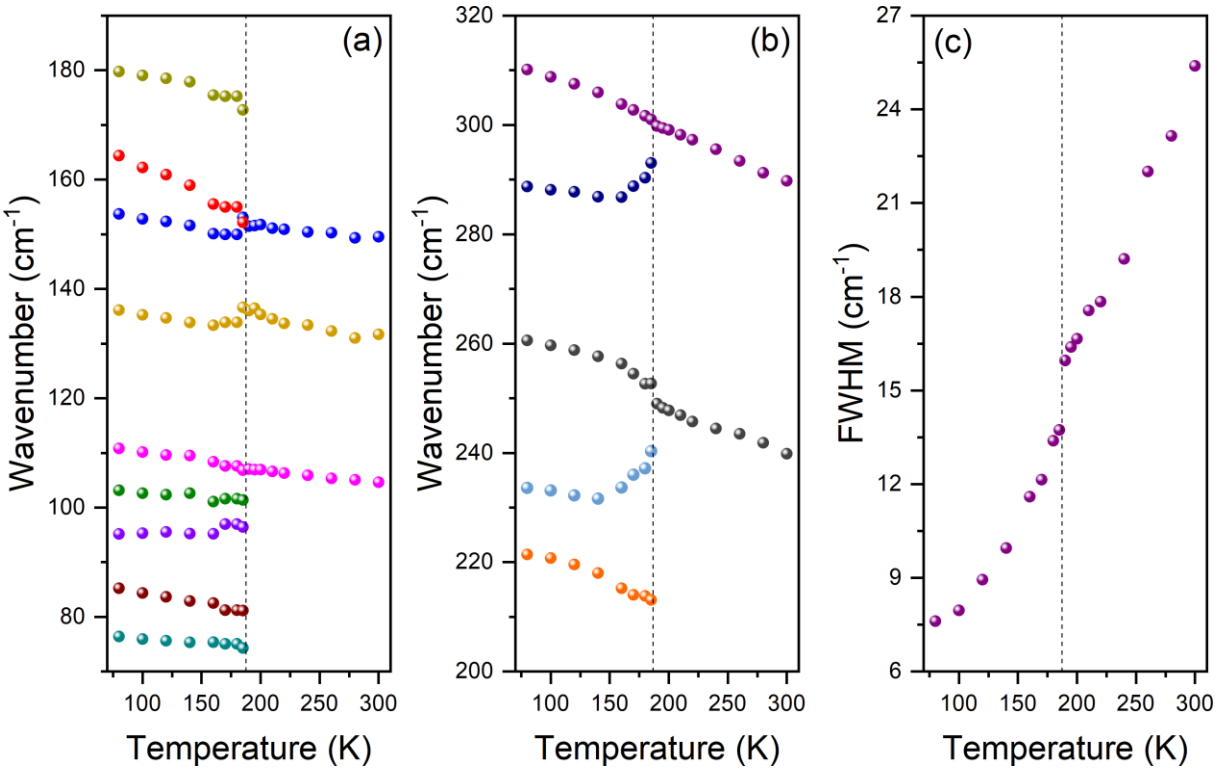

Figure S10. Temperature dependence of wavenumbers for lattice modes (a and b). Panel (c) shows temperature dependence of FWHM for the 290 cm^{-1} lattice mode.

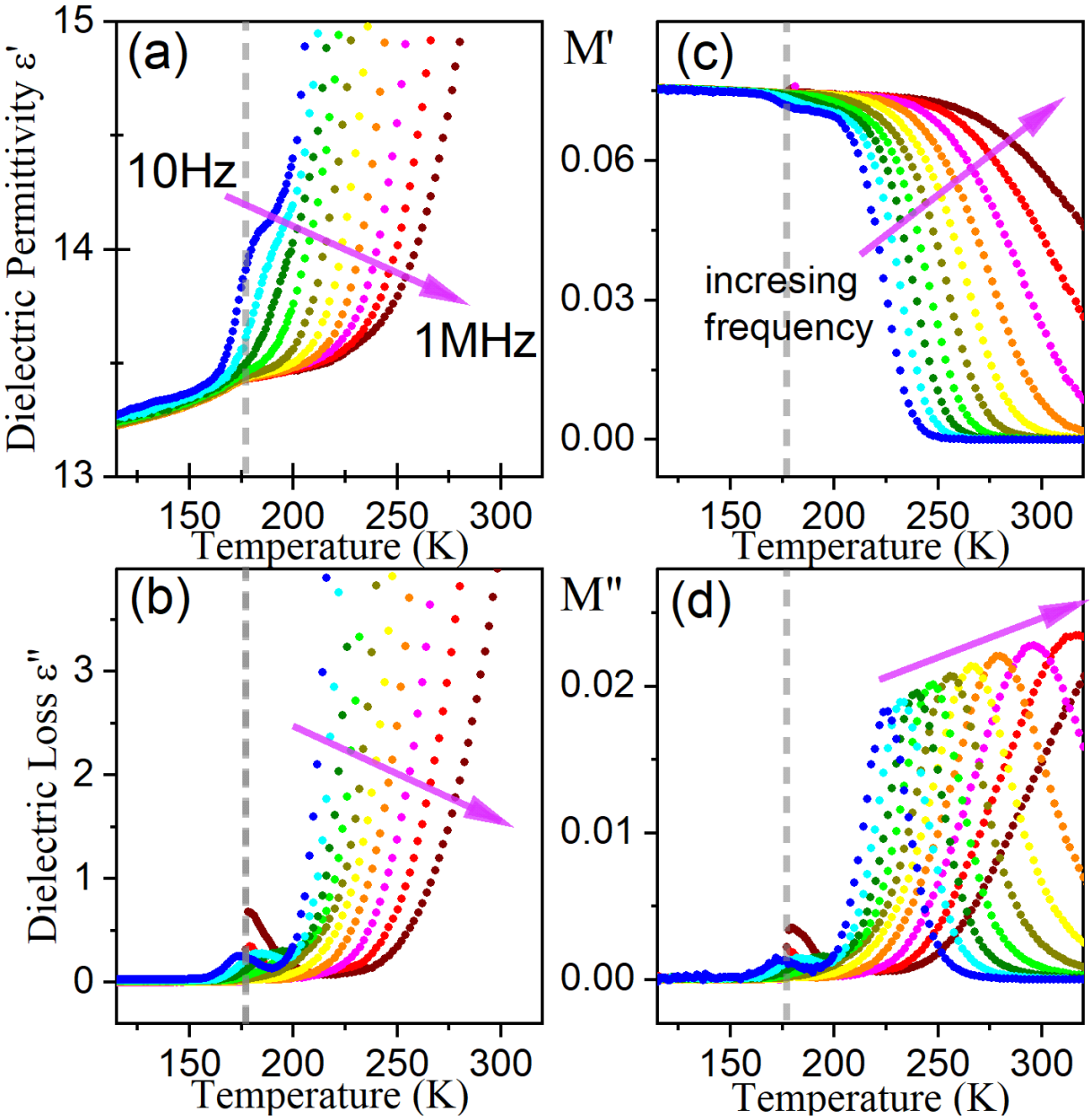

Figure S11. (a) Dielectric permittivity, (b) dielectric loss, (c) real and (d) imaginary components of electric modulus spectra as a function of temperature in [FA]Mn($H_2POO)_3$. The representative curves are plotted in frequency decades between 10 Hz and 1MHz. Dash line corresponds to the phase transition temperature taken from DSC measurements.

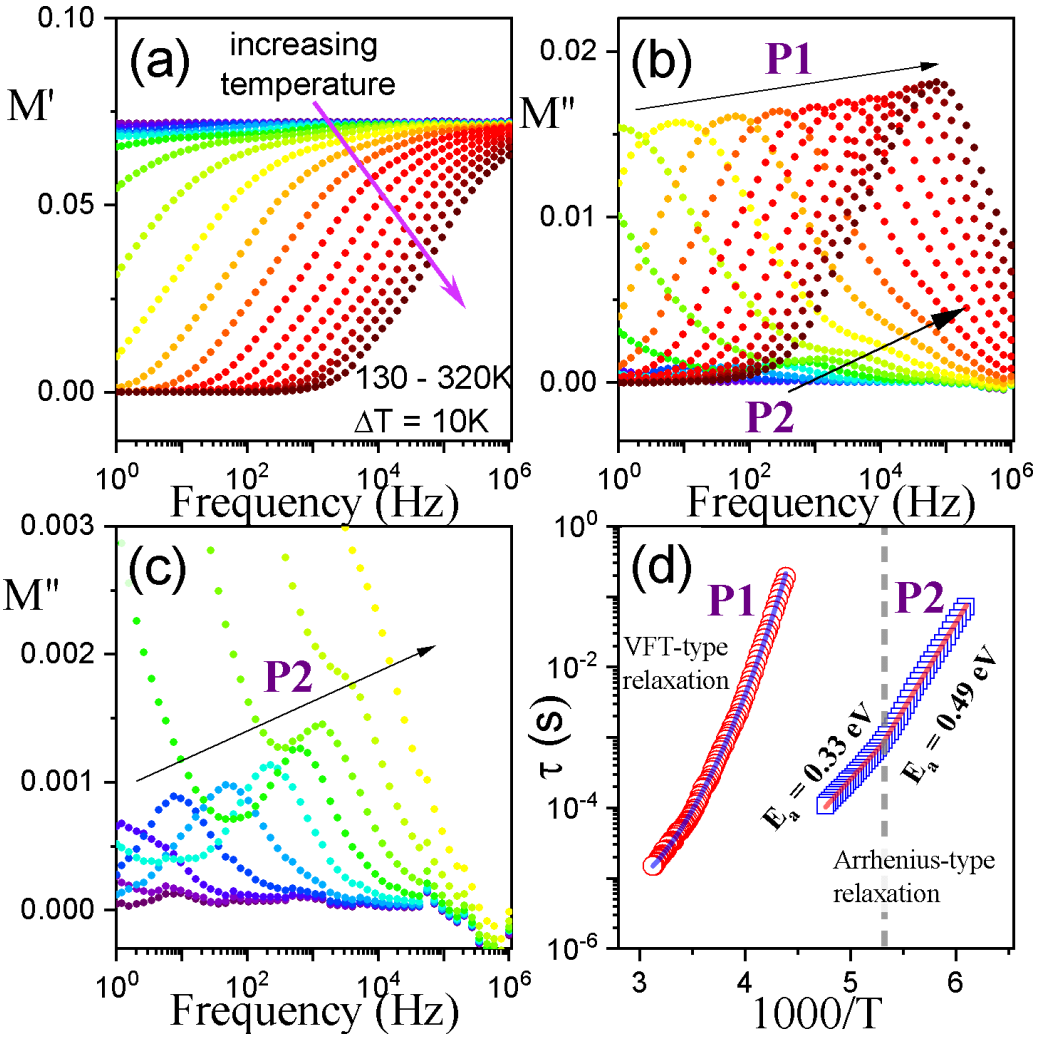

Figure S12. (a) Frequency dependence of M' and (b,c) M" for [FA]Cd(H_2POO)$_3$ sample. The characteristic dipolar relaxation peaks shift to higher frequencies with increasing temperature, P2 process tends to Arrhenius behaviour while P1 process follows the VFT dependence. (d) The estimated relaxation times of FA^+ motion as a function of inverse temperature. Dash line corresponds to the structural phase transition temperature.

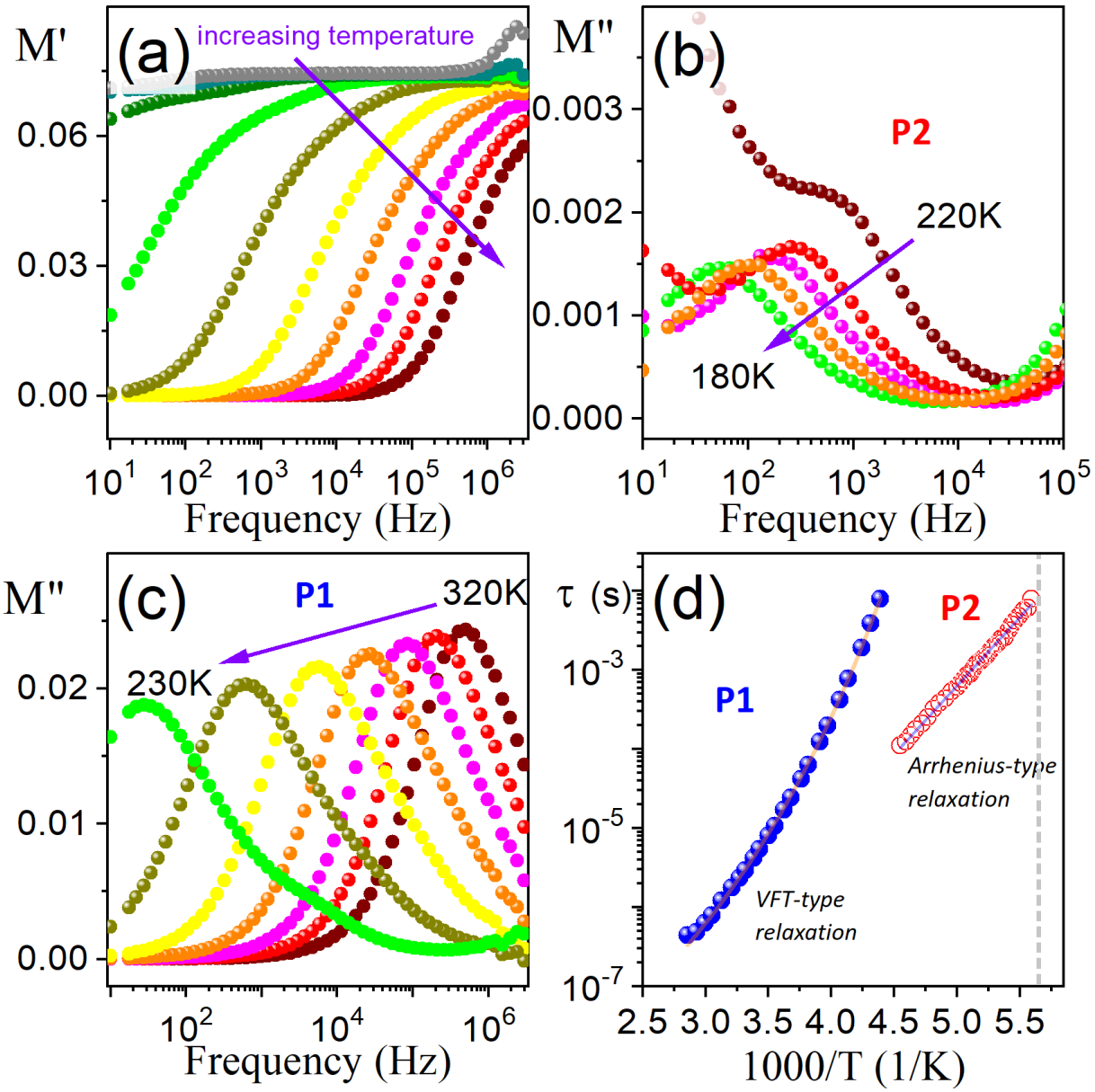

Figure S13. (a) Frequency dependence of M' and (b,c) M" for [FA]Mn($H_2POO)_3$ sample. The characteristic dipolar relaxation peaks shift to higher frequencies with increasing temperature, P2 process tends to Arrhenius behaviour while P1 process follows the VFT dependence. (d) The estimated relaxation times of FA^+ motion as a function of inverse temperature. Dash line corresponds to the structural phase transition temperature.

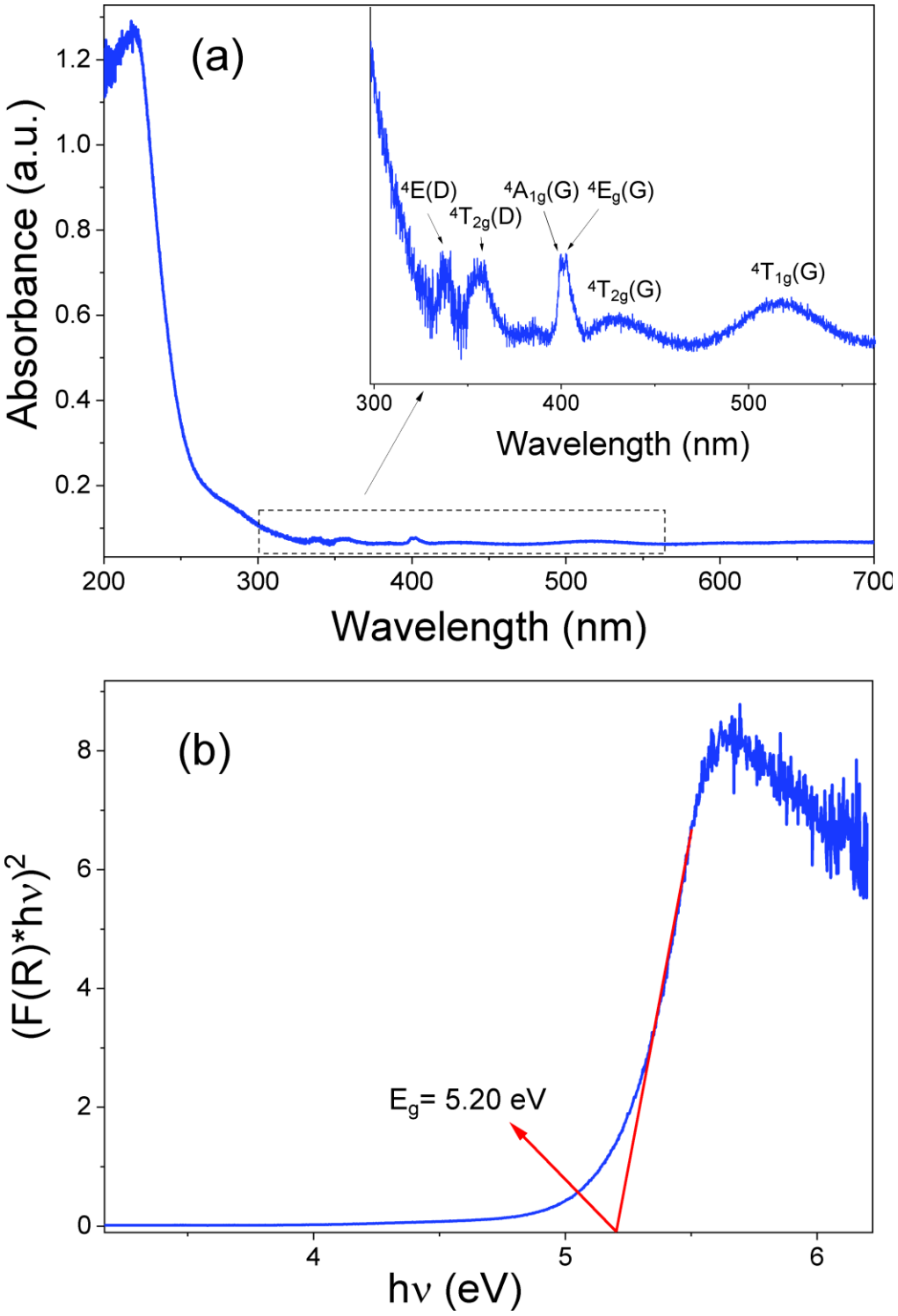

Figure S14. (a) Absorption spectrum of [FA]Mn($H_2POO)_3$ recorded at 300 K and (b) the energy bandgap determined using Kubelka – Munk function.

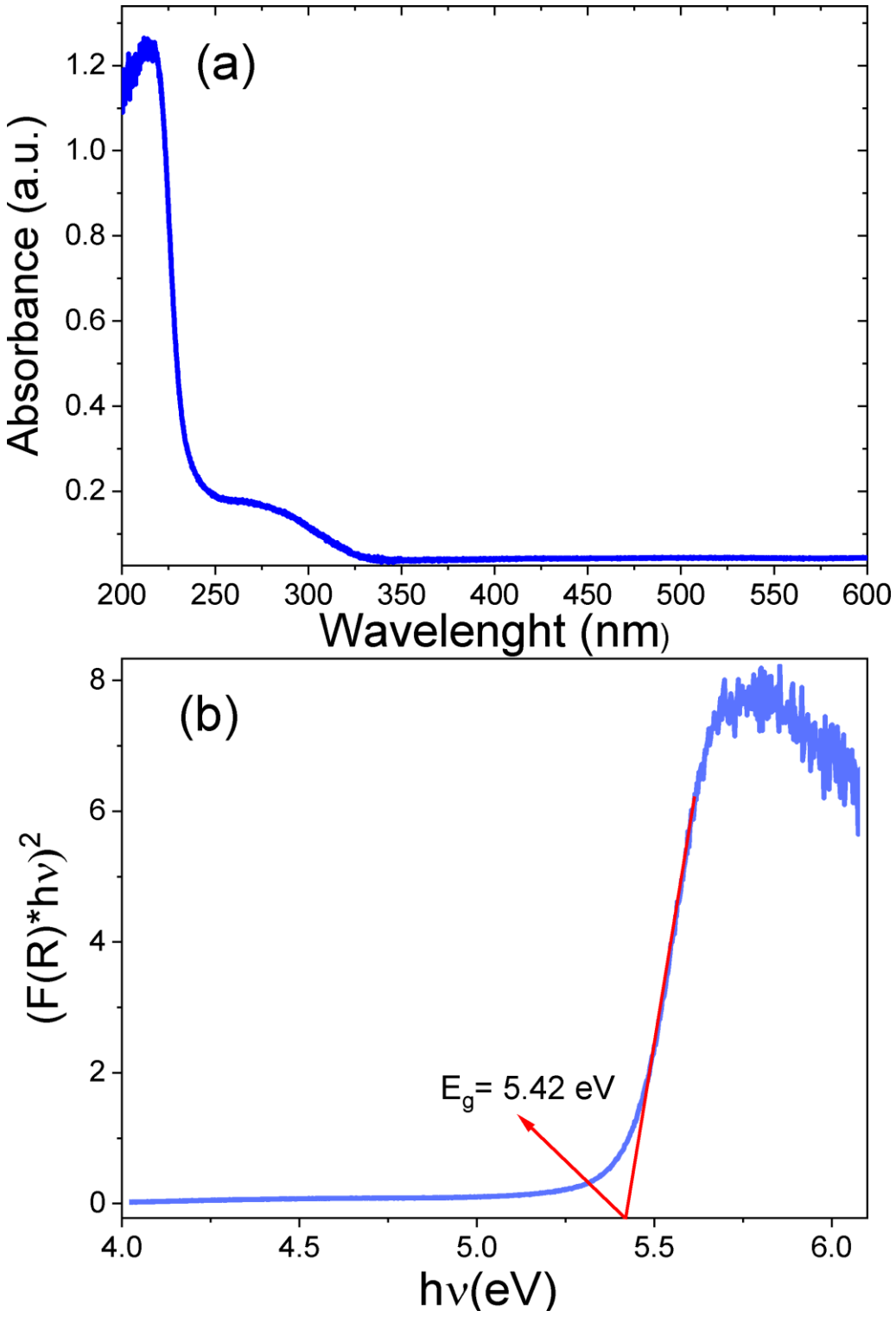

Figure S15. (a) Absorption spectrum of [FA]Cd($H_2POO)_3$ recorded at 300 K and (b) the energy bandgap determined using Kubelka – Munk function.

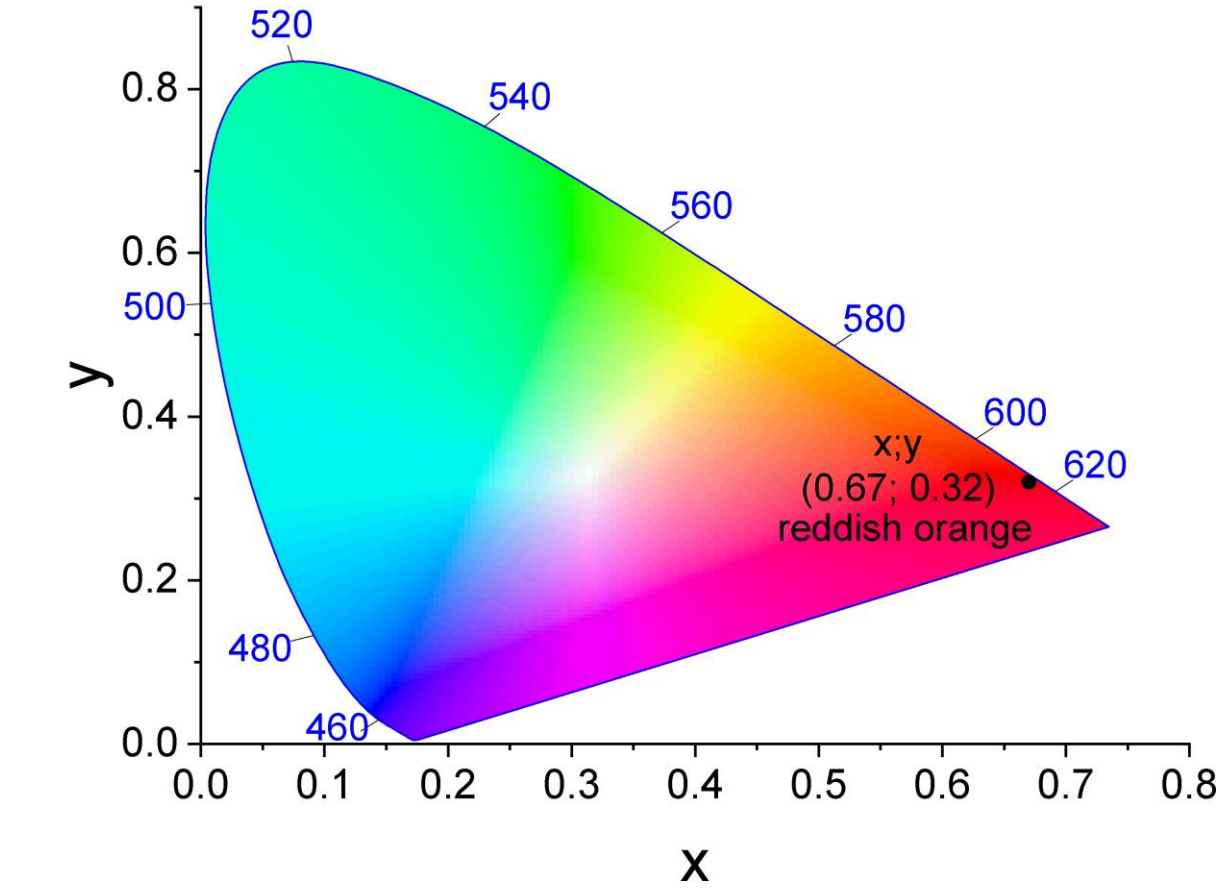

Figure S16. CIE coordinate for [FA]Mn($H_2POO)_3$.

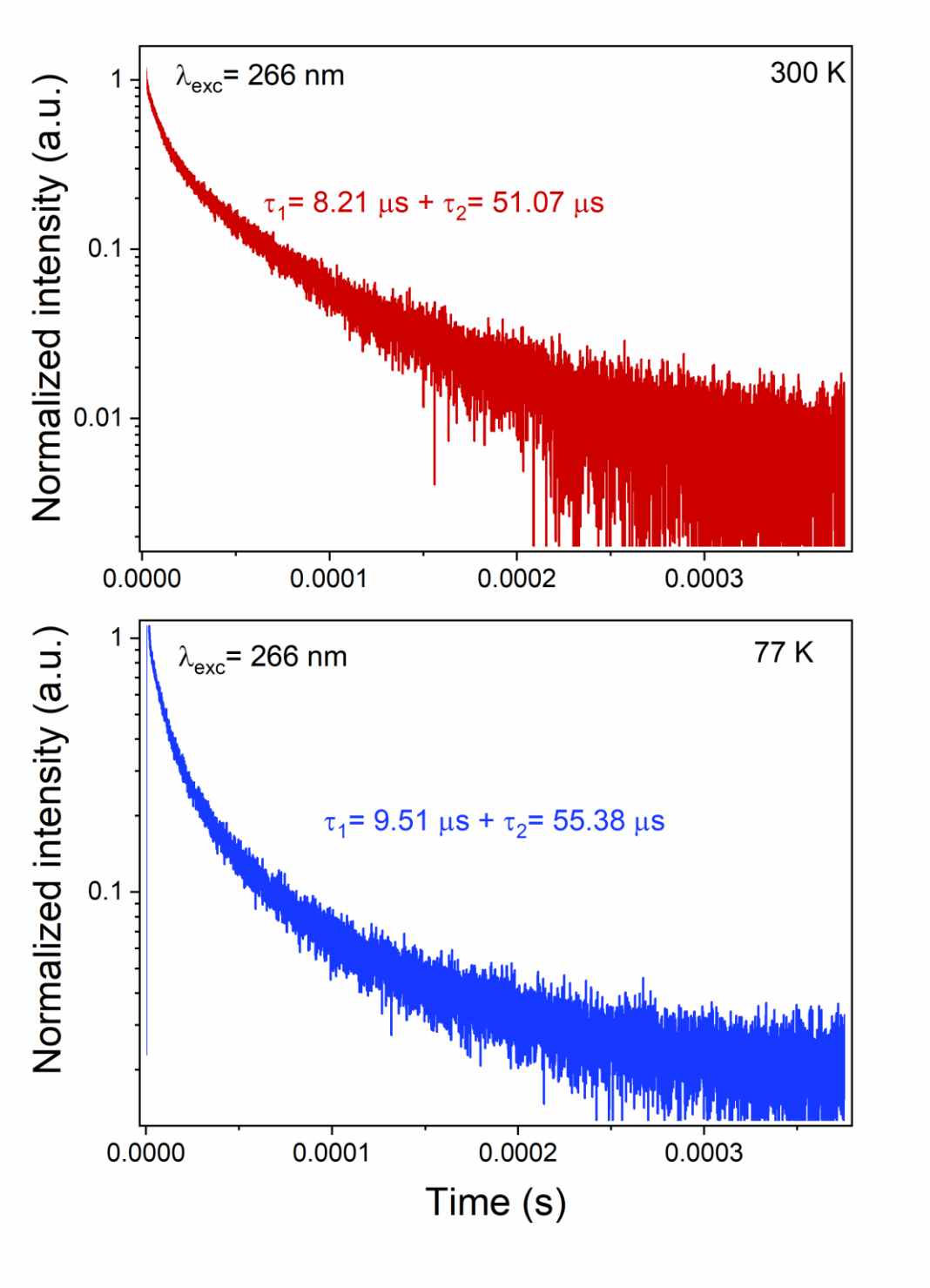

Figure S17. Emission decay curves of [FA]Mn(H_2POO)$_3$ at 77 and 300 K.

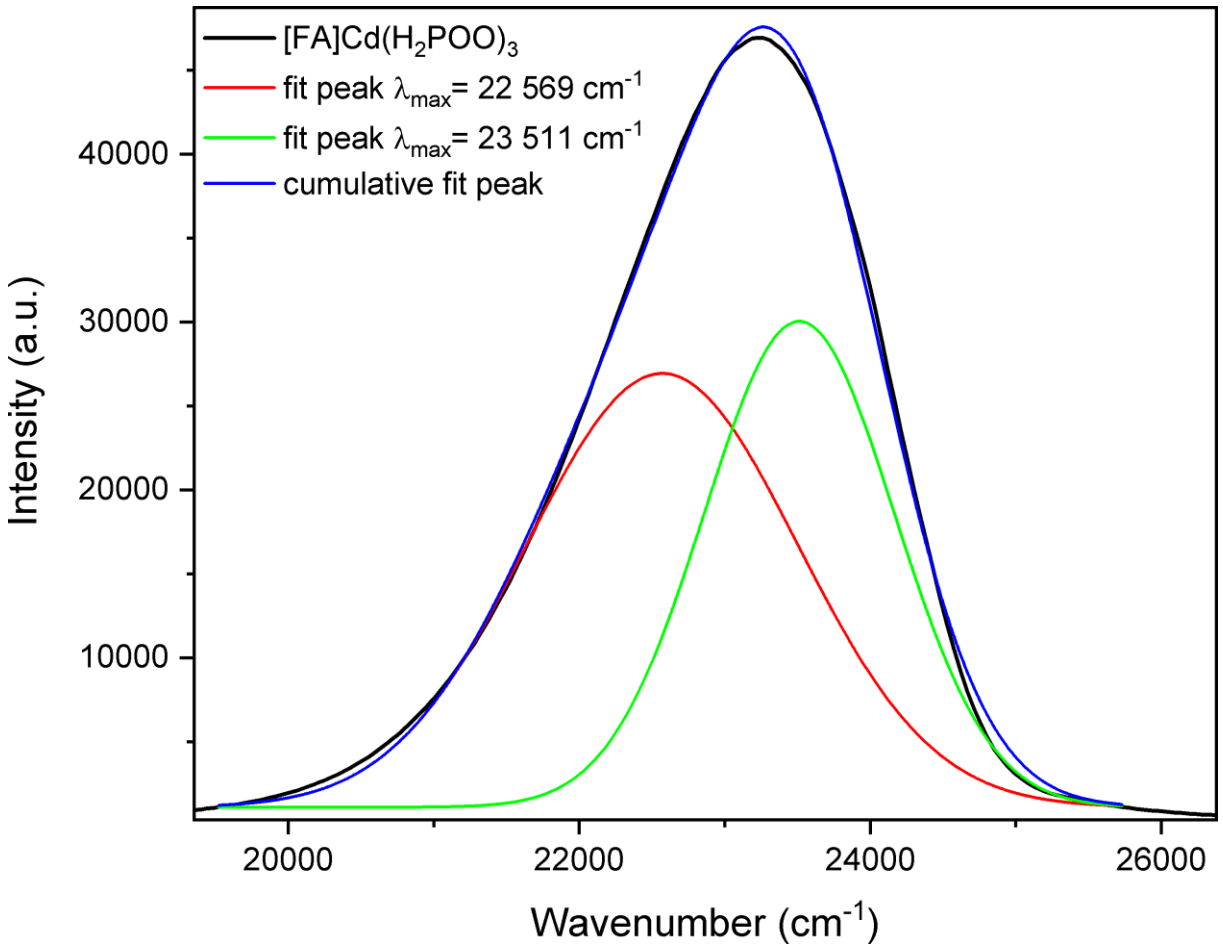

Figure S18. Deconvolution of emission spectrum of [FA]Cd($H_2POO)_3$ recorded under 266 nm at 80 K.

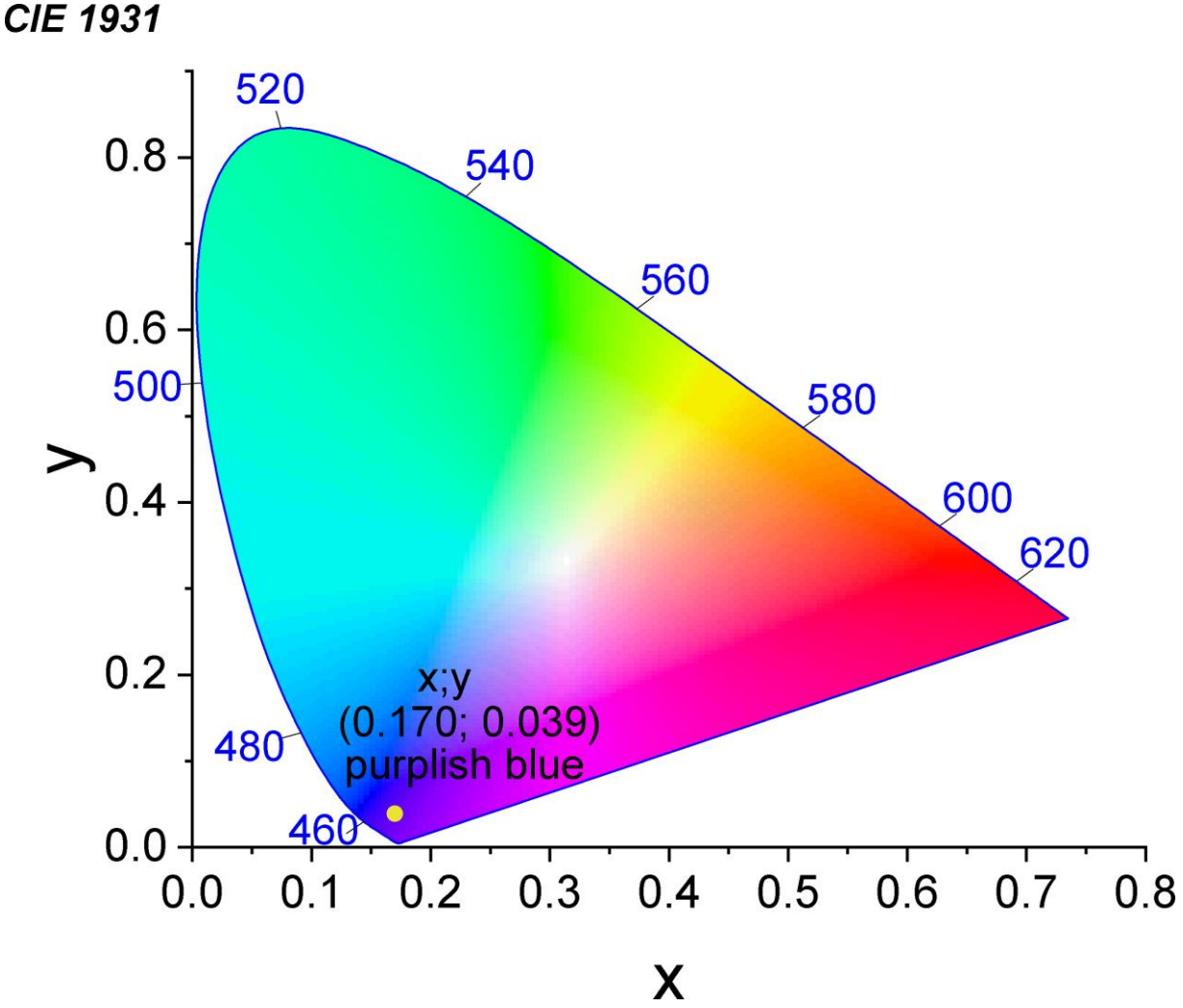

Figure S19. CIE coordinate for [FA]Cd(H_2POO)$_3$.

[1] M. E. Fleet, *Mineral. Mag.*; 1976**, 40**, 531-533.

[2] H. L. B. Boström, J. A. Hill and A. L. Goodwin, *Columnar shifts as symmetry-breaking degrees of freedom in molecular perovskites*, Phys. Chem. Chem. Phys., 2016, 18, 31881–31894.

[3] H. L. B. Boström, *Tilts and shifts in molecular perovskites*, CrystEngComm, 2020, **22**, 961-968.